quently harden the coat. However, this coating method is easily generalized to allow for different ways of hardening the particle coats. With the use of appropriate reagents, this technique is also compatible with schemes that thermally or optically initiate the hardening of the coats. Figure 6 shows confocal images of a polystyrene bead encapsulated with an agarose coat that was hardened by lowering its temperature. In Fig. 7, we show an optical micrograph of a poppy seed encapsulated in a poly(styrenesulfonic acid) coat that was photopolymerized. The selective withdrawal geometry may also be inverted by inserting the straw through the bottom of the withdrawal container, with the straw tip positioned below the interface. Now the denser aqueous fluid is the primary fluid being withdrawn, and the particles to be coated are placed in the oil (upper fluid). This inversion extends the applicability of this coating technique to hydrophobic particles in oil-soluble reagents as well as to heavy particles in the upper fluid that will sediment to the interfacial boundary.

The selective withdrawal coating technique complements other currently available techniques, such as surface-induced polymerization (*10*), which can also produce coats of uniform thickness on irregularly shaped particles but which often require modification of the particle surface and therefore may not be feasible. In our technique, as illustrated in the description of the polyamide coating, the particles can be completely separated from the caustic reagents that initiate the polymerization at the outer interface. Moreover, surface-induced polymerization requires the reagent to be stable in the solution being polymerized. This is not always possible (as with the polyamide coat installation, the trichloride reagent is unstable in aqueous solutions), and selective withdrawal can solve this problem by initiating polymerization with a reagent that is stable in the fluid surrounding the coat. Finally, many polymer coatings are either difficult [e.g., the photopolymerized poly(styrenesulfonic acid) coat shown in Fig. 7] or impossible (e.g., the thermally hardened agarose coat shown in Fig. 6) to prepare using techniques such as surface-induced polymerization and must be hardened in bulk. For these cases in particular, selective withdrawal presents a valuable advantage over currently available coating techniques.

The selective withdrawal technique can be readily optimized. With a single tube we estimate that 10,000 particles can be coated per hour. Preliminary experiments have demonstrated that this technique can be scaled up by using an array of tubes in parallel. Injecting particles directly into the region below the spout can make the method suitable for particles with higher density than the prepolymer. As described above, inversion of the selective withdrawal geometry can extend the applicability of this technique to hydrophobic particles in oil-soluble reagents. Because of its flexibility in polymerization schemes, its ability to coat particles of many different types, and its ability to tune the thickness of the coats, this technique is an attractive option in a range of applications and a valuable addition to the repertoire of currently available coating techniques.

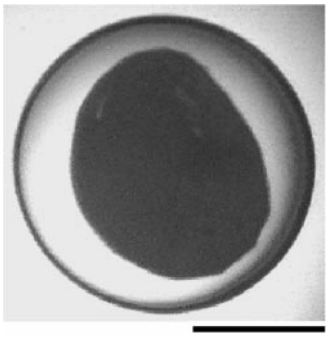

Fig. 7. Optical micrograph of a poppy seed encapsulated in a poly(styrenesulfonic acid) coat. The poppy seed appears as a dark solid object 0.9 mm in diameter; the coat is 0.2 mm thick. The prepolymer used is styrene sulfonic acid sodium salt (30% w/v in D_2O) and triethylene glycol diacrylate (5% w/v in D_2O) mixed with eosin Y (0.5 mM) and triethanolamine (100 mM) as the photosensitizer–electron donor initiating system (*18*). After the selective withdrawal process, the coated particles were collected in a plastic container and irradiated for 20 min with a halogen lamp. Scale bar, 0.5 mm.

References and Notes

1. A. J. Mendonca, X. Y. Xiao, *Med. Res. Rev.* **19**, 451 (1999).
2. S. J. Shuttleworth, S. M. Allin, P. K. Sharma, *Synthesis* **11**, 1217 (1997).
3. F. Lim, A. M. Sun, *Science* **210**, 908 (1980).
4. P. Soon-Shiong, *Adv. Drug Deliv. Rev.* **35**, 259 (1999).
5. R. Langer, *Acc. Chem. Res.* **33**, 94 (2000).
6. G. H. J. Wolters, W. M. Fritschy, D. Gerrits, R. Van Schilfgaarde, *J. Appl. Biomater.* **3**, 281 (1992).
7. T. Yoshioka, R. Hirano, T. Shioya, M. Kako, *Biotechnol. Bioeng.* **35**, 66 (1990).
8. E. Mathiowitz, *Encyclopedia of Controlled Drug Delivery* (Wiley, New York, 1999).
9. E. Donath, G. B. Sukhorukov, F. Caruso, S. A. Davis, H. Mohwald, *Angew. Chem. Int. Ed.* **37**, 2202 (1998).
10. G. M. Cruise, O. D. Hegre, D. S. Scharp, J. A. Hubbell, *Biotechnol. Bioeng.* **57**, 655 (1998).
11. J. R. Lister, *J. Fluid Mech.* **198**, 231 (1989).
12. S. Blake and G. N. Ivey, *J. Volcanol. Geotherm. Res.* **27**, 153 (1986).
13. I. Cohen and S. R. Nagel, in preparation.
14. E. E. Timm, U.S. Patent 4,444,961 (1984).
15. Even without the inclusion of particles, as originally shown by Savart [*Annal. Chim.* **53**, 337 (1883)] and Rayleigh [*Philos. Mag.* **34**, 177 (1892)], the prepolymer spout will break into droplets that can be hardened, allowing the fabrication of monodisperse particles.
16. A. M. Ganan-Calvo, *Phys. Rev. Lett.* **80**, 285 (1997).
17. P. B. Umbanhowar, V. Prasad, D. A. Weitz, *Langmuir* **16**, 347 (2000).
18. O. Valges-Aguilera, C. P. Pathak, J. Shi, D. Watson, D. C. Neckers, *Macromolecules* **25**, 541 (1992).

19. We thank H. Rilo and A. Rotamel for early discussions that motivated these studies. We also thank C. Lassy and the Confocal Digital Imaging Facility at the University of Chicago. Supported by NSF grant DMR-9722646 and NSF Materials Research Science and Engineering Centers Program grant DMR-9808595.

19 January 2001; accepted 7 March 2001

Anthropogenic Warming of Earth's Climate System

Sydney Levitus,[1]* John I. Antonov,[1] Julian Wang,[2] Thomas L. Delworth,[3] Keith W. Dixon,[3] Anthony J. Broccoli[3]

We compared the temporal variability of the heat content of the world ocean, of the global atmosphere, and of components of Earth's cryosphere during the latter half of the 20th century. Each component has increased its heat content (the atmosphere and the ocean) or exhibited melting (the cryosphere). The estimated increase of observed global ocean heat content (over the depth range from 0 to 3000 meters) between the 1950s and 1990s is at least one order of magnitude larger than the increase in heat content of any other component. Simulation results using an atmosphere-ocean general circulation model that includes estimates of the radiative effects of observed temporal variations in greenhouse gases, sulfate aerosols, solar irradiance, and volcanic aerosols over the past century agree with our observation-based estimate of the increase in ocean heat content. The results we present suggest that the observed increase in ocean heat content may largely be due to the increase of anthropogenic gases in Earth's atmosphere.

Studies using instrumental data to document a warming of Earth's climate system due to increasing concentrations of greenhouse gases (GHGs) have focused on surface air temperature and sea surface temperature (*1*). These variables have proved invaluable for documenting an average warming of approximately 0.6°C at Earth's surface (*1*) during the past 100 years. Recent comparisons (*2–4*) with paleoclimatic proxy data indicate that

the observed increase in surface temperature during the past century is unprecedented during the past 1000 years. The results of these studies, in conjunction with similar results found using general circulation model (GCM) and energy balance model studies (*5*–*8*) that include forcing by the observed time-dependent increase in GHGs and sulfate aerosols, as well as changes in solar irradiance and volcanic aerosols, provide evidence that the warming of Earth's surface during the past few decades is of anthropogenic origin. Despite the agreement between models and observations, it is conceivable that some of the surface warming might be compensated for by a cooling of other parts of Earth's climate system. Conversely, additional warming may be occurring in other parts of the climate system, such as the recently observed warming of the world ocean (*9*).

Here we address these issues by quantifying the primary components of the heat balance of the Earth system. We document a warming of Earth's climate system during the latter half of the 20th century, based on increases in the heat content of the atmosphere and ocean, as well as estimates of the total heat of fusion associated with the partial melting of several components of Earth's cryosphere. Further, we compare these changes with increases in ocean heat content simulated by an atmosphere-ocean GCM (AOGCM) that is forced with estimates of the radiative effects of observed temporal variations in atmospheric GHGs, the direct effect of sulfate aerosols, solar irradiance, and volcanic aerosols over the past century.

The estimated temporal variability of global ocean and atmospheric heat content, based on instrumental data for the 1955–96 period, is shown in Fig. 1. The ocean heat content time series (calculated for the global ocean over the depth range from 0 to 3000 m) and its computation were recently described (*9*). The atmospheric sensible heat content is based on the National Centers for Environmental Protection/National Center for Atmospheric Research (NCEP/NCAR) reanalysis fields (*10*). The ocean heat content curve is based on analyses of 5-year running composites of historical ocean data. The atmospheric heat content is shown as anomalies averaged for 1-year periods. Other components of atmospheric energy change, associated with changes in the latent heat of evaporation and geopotential height field, are an order of magnitude smaller than the change in sensible heat in the NCEP/NCAR analyses. The increase in observed ocean heat content is 18.2×10^{22} J (based on the linear trend for the 1957–1994 period but prorated to 1955–1996), whereas the increase in atmospheric heat content is more than an order of magnitude smaller: 6.6×10^{21} J.

The melting and freezing of land and sea ice are physical processes that can act as sources or sinks of heat with respect to the atmosphere and ocean components of Earth's climate system. On the basis of estimates of the changes in the areal extent, thickness, or volume of these components of Earth's cryosphere, we estimate the total latent heat of fusion (*11*–*13*) that corresponds to their partial melting since approximately 1950. Such estimates require additional assumptions, such as assigning a salinity and temperature to the sea ice that melted or estimating the total amount of ice that has melted. We document the assumptions made in each of our estimates of cryospheric change (Table 1). We emphasize that we make assumptions that will produce relatively high estimates of the total heat of fusion that can be associated with the melting of these parts of the cryosphere, and

[1]National Oceanographic Data Center/National Oceanic and Atmospheric Administration (NODC/NOAA), [2]Air Resources Laboratory, NODC/NOAA, E/OC5, 1315 East-West Highway, Silver Spring, MD 20910, USA. [3]Geophysical Fluid Dynamics Laboratory/NOAA, Post Office Box 308, Princeton, NJ 08542, USA.
*To whom correspondence should be addressed. E-mail: slevitus@nodc.noaa.gov

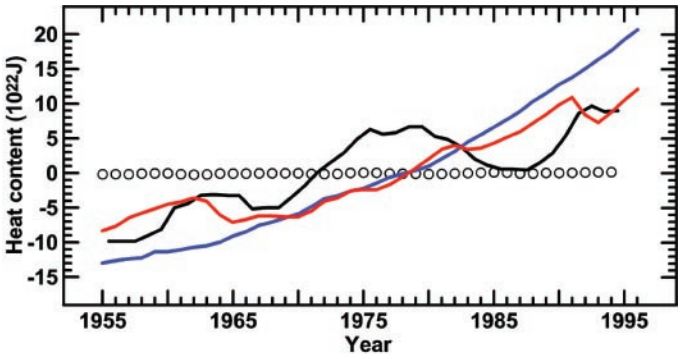

Fig. 1. Time series of various components of the observed and simulated global heat content (units are 10^{22} J). The observed global (calculated over the depth range from 0 to 3000 m) ocean heat content (*9*) is shown in black; the open circles denote the observed global mean atmospheric heat content (*10*). The red curve denotes the ensemble mean global ocean heat content from a set of three simulations (experiment GSSV) using a coupled ocean-atmosphere model. The model incorporates estimates of the radiative effects of past changes in GHGs, sulfate aerosols, solar irradiance, and volcanic aerosols. The blue curve denotes the same for an additional set of three simulations (experiment GS), which is similar to experiment GSSV except that the radiative effects of changes in solar irradiance and volcanic aerosols are omitted. For the two model curves, their respective means for 1955–1996 were removed before plotting. Note that 1.5×10^{22} J equals 1 watt–year m^{-2} (averaged over the entire surface of Earth).

Table 1. Comparison of the heat balance of the climate system.

Component of the climate system and source of data	Time period of change	Observed or estimated change	Assumption made in this calculation	Heat content increase or total heat of fusion
World ocean (*5*)	1955–1996	Observed temperature increase	–	18.2×10^{22} J
Global atmosphere (*6*)	1955–1996	Observed temperature increase	–	6.6×10^{21} J
Decrease in the mass of continental glaciers (*1*)	1955–1996	–	Assumed 1.8 mm per year increase in sea level	8.1×10^{21} J
Decrease in Antarctic sea ice extent (*18*)	1950s–1970s	Estimated 311-km reduction in sea ice edge	$\rho_i = 9.17 \times 10^{11}$ kg km^{-3} $\lambda_i = 3.34 \times 10^5$ J kg^{-1} 100% ice coverage of 2-m thickness	3.2×10^{21} J
Mountain glacier decrease (*14*)	1961–1997	3.7×10^3 km^3 decrease in mountain glacier ice volume	$\rho_i = 9.17 \times 10^{11}$ kg km^{-3} $\lambda_i = 3.34 \times 10^5$ J kg^{-1}	1.1×10^{21} J
Decrease in Northern Hemisphere sea ice extent (*17*)	1978–1996	Areal change based on satellite measurements	100% ice coverage of 2-m thickness	4.6×10^{19} J
Decrease in Arctic perennial sea ice volume (*16*)	1950s–1990s	40% decrease in sea ice thickness	Thickness of the melted sea ice = 1.3 m $\rho_i = 9.17 \times 10^{11}$ kg km^{-3} $\lambda_i = 3.34 \times 10^5$ J kg^{-1}	2.4×10^{19} J

that we are simply making "order-of-magnitude" estimates of these terms. Our results will demonstrate that for the purpose of determining which components of Earth's climate system dominated as sinks or sources of heat between the 1950s and 1990s, these assumptions are not critical. This is because the change in ocean heat content was by far the dominant sink of heat during this period.

Estimates of the melting of continental glaciers (Antarctica and Greenland) range from –1.8 to 1.8 mm of global sea level change per year (*1*). Using a value of 1.8 mm per year, the amount of heat required to melt continental glacier ice corresponding to this increase in sea level during a 41-year period is 8.1×10^{21} J.

The most recent estimates of mountain glacier variability document that the "loss of glacier volume has been more or less continuous since the 19th century" (*14*). During the 1961–1997 period, there was a loss of 3.7×10^3 km^3 of mountain glacier volume. We compute a value of 1.1×10^{21} J for the amount of heat required to melt this volume of freshwater ice.

A 40% decrease in the thickness of perennial Arctic sea ice during the past 40 years has recently been estimated from ice draft measurements made from nuclear submarines (*15*, *16*). Assuming an area of 6.85×10^4 km^2 for ice extent, the observed decrease in ice thickness of 1.3 m (*16*) corresponds to a decrease in ice volume of 8.9×10^4 km^3. The amount of heat required to melt this volume of sea ice is 2.4×10^{19} J.

A net decrease in the areal coverage of Northern Hemisphere sea ice cover from 1978 to 1996 has been estimated from satellite measurements (*17*). Assuming that the area of decreased sea ice extent had 100% coverage of 2-m-thick sea ice, we estimate a total latent heat of fusion of 4.6×10^{19} J.

A decline in Antarctic sea ice extent has been suggested to have occurred between the early 1950s and the mid-1970s (*18*). The validity of this estimate has been questioned (*19*), and we cannot resolve this issue. As we shall see, this contribution, if real, represents only a minor contribution to Earth's heat balance during the 1955–96 period. Based on recently available historical whaling records, which provide a record of circumpolar sea ice extent, it is now estimated that the Antarctic sea ice boundary retreated poleward by an average of 2.8° of latitude between the 1950s and 1970s, whereupon the boundary stabilized. Assuming that the area of decreased sea ice extent had 100% coverage of 2-m-thick sea ice, a maximum of 3.2×10^{21} J of latent heat of fusion is associated with this change.

Our analysis of components of Earth's heat balance quantitatively demonstrates that during the latter half of the 20th century, changes in ocean heat content dominate the changes in Earth's heat balance.

The observed increase in oceanic heat content is compared to changes in ocean heat content from a coupled model of Earth's climate system. The coupled ocean-atmosphere-ice model used, developed at the Geophysical Fluid Dynamics Laboratory (GFDL), is higher in spatial resolution than an earlier version used in many previous studies of climate variability and change (*20*, *21*) but employs similar physics. The coupled model is global in domain and consists of GCMs of the atmosphere (spectral model with rhomboidal 30 truncation, corresponding to an approximate resolution of 3.75° longitude by 2.25° latitude, with 14 vertical levels) and ocean (1.875° longitude by 2.25° latitude, with 18 vertical levels). The model atmosphere and ocean communicate through fluxes of heat, water, and momentum at the air-sea interface. Flux adjustments (which did not vary interannually) are used to facilitate the simulation of a realistic mean state. Over oceanic regions, a thermodynamic sea ice model is used that includes the advection of ice by surface ocean currents.

Results are presented from two ensembles of integrations (each of which has three members). In the first ensemble (denoted GSSV), the radiative effects of the observed temporal variations in GHGs, sulfate aerosols, solar irradiance, and volcanic aerosols over the past century are included (*22*). The ensemble members differ in their initial conditions, which are chosen from widely separated points in a 900-year-long control integration. The second ensemble (denoted GS) differs from the first by omitting the radiative effects of changes in solar irradiance and volcanic aerosols, while retaining the effects of changes in GHGs and sulfate aerosols.

The global ocean heat content (calculated over the depth range from 0 to 3000 m) for the GSSV ensemble is shown in Fig. 1. Based on a linear trend, the simulated heat content increased by 19.7×10^{22} J over the period 1955 to 1996. This is in excellent agreement with the observed estimate (18.2×10^{22} J). However, it must be stressed that substantial uncertainties exist in the specification and parameterizations of the model radiative forcing, particularly with respect to the effects of sulfate aerosols and volcanic activity. In addition, the ocean heat content estimates are based on a data set characterized by coverage that varies with time (*23*). Thus, the close agreement between the simulated and observed ocean heat content increases must be evaluated in the light of these uncertainties. Nevertheless, this agreement is extremely encouraging with respect to the ability of the GFDL AOGCM to simulate the observed multidecadal changes in the heat balance of the ocean.

The second ensemble of integrations (GS) differs from the first by omitting the radiative effects of changes in solar irradiance and volcanic aerosols. As shown in Fig. 1, the simulated increase of ocean heat content in GS is approximately 70% larger than in GSSV or than the observed estimate. Based on an additional set of experiments (*24*), the difference in ocean heat content increase between GSSV and GS is primarily due to the radiative effects of volcanic activity. The difference between GSSV and GS highlights the important role that volcanic activity appears to play in ocean heat content during the late 20th century. In the GSSV ensemble, volcanoes contributed an average global adjusted radiative forcing of -0.5 W m^{-2} at the tropopause over the period 1960–1999 (*25*). This offsets an important fraction of the anthropogenic forcing during the same period.

It is important to evaluate whether the trend in simulated ocean heat content from the 1950s to the 1990s for ensemble GSSV (Fig. 1) could arise purely from internal variability of the coupled ocean-atmosphere system. To assess this, all possible 41-year trends were calculated in a 900-year integration of the coupled model without the radiative effects of changes in GHGs, sulfate aerosols, solar irradiance, and volcanic aerosols. No simulated 41-year trend in that integration (out of 860 possible 41-year trends) was as large as that simulated in any of the three ensemble members over the period 1955–1996, thereby demonstrating that the simulated trends in ocean heat content could not arise (in this model) solely from interactions within the ocean-atmosphere-ice system. The simulated trends require a sustained, positive thermal forcing, such as that expected from increasing concentrations of GHGs.

Although there is excellent agreement between the simulated and observed ocean heat content increases over the long term (from the 1950s to the 1990s), substantial differences exist on the decadal scale. In particular, simulated decadal variations are smaller in amplitude than the observed variations, and there are differences in phase. The causes of these differences need to be identified. Possible causes include an underestimation by the model of the internal variability of the ocean-atmosphere system on decadal scales and uncertainties in the estimates of past radiative forcing. Inadequacies in the ocean observational data may also play a role.

Our observational results make clear that each individual component of Earth's climate system that we have examined has warmed over the latter half of the 20th century and that the dominant change in heat content is associated with the warming of the world ocean. The agreement between our model results and observational estimates of ocean heat content supports the hypothesis that increases in radiative forcing are the source of the warming observed between 1955 and

1996. Because most of the increase in radiative forcing in the latter half of the 20th century is anthropogenic, this suggests a possible human influence on observed changes in climate system heat content.

References and Notes

1. Intergovernmental Panel on Climate Change, *Climate Change 1995: The Science of Climate Change, the Contribution of Working Group 1 to the Second Assessment Report of the Intergovernmental Panel on Climate Change* (Cambridge Univ. Press, Cambridge, 1996).
2. M. E. Mann, R. S. Bradley, M. K. Hughes, *Nature* **392**, 779 (1998).
3. _____, *Geophys. Res. Lett.* **26**, 759 (1999).
4. K. R. Briffa, P. D. Jones, F. H. Schweingruber, S. G. Shiyatov, E. R. Cook, *Nature* **376**, 156 (1995).
5. S. F. B. Tett *et al.*, *Nature* **399**, 569 (1999).
6. T. J. Crowley, *Science* **289**, 270 (2000).
7. T. L. Delworth, T. R. Knutson, *Science* **287**, 2246 (2000).
8. P. A. Stott *et al.*, *Science* **290**, 2133 (2000).
9. S. Levitus, J. I. Antonov, T. P. Boyer, C. Stephens, *Science* **287**, 2225 (2000).
10. E. Kalnay *et al.*, *Bull. Am. Meteorol. Soc.* **77**, 11 (1996).
11. The total heat of fusion, ΔH_i (J), associated with the melting of ice as $\Delta H_i(T_i, S_i) = (\rho_i)(\lambda_i)(\Delta V_i)$, in which ρ_i (T_i, S_i) = the density (in kg m^{-3}) of ice with salinity S_i and temperature T_i; λ_i (T_i, S_i, ν_a) = the latent heat of fusion (in J kg^{-1}) of sea ice, which is defined as the amount of heat required to melt 1 kg of sea ice with initial salinity S_i and temperature T_i and containing an amount of air given by ν_a; ΔV_i = total ice volume. The density and latent heat of fusion of freshwater ice are 910 kg m^{-3} and 3.34 $\times$ 10^5 J kg^{-1}, respectively (*12*). We do not take the variability of air content into account because such information is not available.
12. J. A. Curry, P. J. Webster, *Thermodynamics of Atmospheres and Oceans* (Academic Press, New York, 1999).
13. N. Ono, in *International Conference on Low Temperature Science: Physics of Snow and Ice*, H. Oura, Ed. (Institute of Low Temperature Science, Hokkaido University, Sapporo, Japan, 1967), vol. 1, pp. 599–610.
14. M. B. Dyuregov, M. F. Meier, *Proc. Natl. Acad. Sci. U.S.A.* **97**, 1406 (2000).
15. W. Lyon, in *International Conference on Low Temperature Science: Physics of Snow and Ice*. H. Oura, Ed. (Institute of Low Temperature Science, Hokkaido University, Sapporo, Japan, 1967), vol. 1, pp. 707–711.
16. D. A. Rothrock, Y. Yu, G. A. Maykut, *Geophys. Res. Lett.* **26**, 3469 (1999).
17. C. L. Parkinson, D. J. Cavalieri, P. Gloersen, H. J. Zwally, J. Comiso, *J. Geophys. Res. Oceans* **104**, 20837 (1999).
18. W. K. de la Mare, *Nature* **389**, 57 (1997).
19. S. Vaughn, *Polar Rec.* **36**, 345 (2000).
20. S. Manabe, R. J. Stouffer, M. J. Spelman, K. Bryan, *J. Clim.* **4**, 785 (1991).
21. S. Manabe, R. J. Stouffer, *J. Clim.* **7**, 5 (1994).
22. The effects of greenhouse gas changes are expressed as changes in CO_2 that would yield a radiative forcing equivalent to that of CO_2, CH_4, N_2O, and chlorofluorocarbons combined. The direct effects of anthropogenic sulfate aerosol are represented by changes in surface albedo (*26, 27*). Variations in solar irradiance are prescribed directly from a recent reconstruction (*28*). Volcanic effects are represented by latitude-dependent perturbations in incident solar radiation, based on estimates of temporal variations in the radiative forcing due to volcanic aerosols in the stratosphere (*25*).
23. S. Levitus *et al., World Ocean Database 1998a, Vol. 1: Introduction. NOAA Atlas NESDIS, Vol. 18* (U.S. Government Printing Office, Washington, DC, 1998). This atlas presents yearly distributions of the locations of all temperature profiles used in preparing the observed estimates of ocean heat content. All data used in the estimation of the observed ocean heat content and the anomaly fields themselves are available online via the NODC Web site (www.nodc.noaa.gov).
24. S. Levitus *et al.*, data not shown.
25. N. G. Andronova, E. V. Rozanov, F. Yang, M. E. Schlesinger, G. L. Stenchikov, *J. Geophys. Res.* **104** (1999).
26. J. F. B. Mitchell, T. C. Johns, J. M. Gregory, S. F. B. Tett, *Nature* **376**, 501 (1995).
27. J. M. Haywood, R. J. Stouffer, R. T. Wetherald, S. Manabe, V. Ramaswamy, *Geophys. Res. Lett.* **24**, 1335 (1997).
28. J. L. Lean, *Geophys. Res. Lett.* **27**, 2425 (2000).

29. This work has been made possible by the efforts of many scientists, science managers, institutions, and governments, as well as by the International Council of Scientific Unions and the Intergovernmental Oceanographic Commission, which support the World Data Center (WDC) System. The WDC system supports the free and open exchange of geophysical data, which is a necessary condition for the development of the global environmental databases needed to study Earth's climate system and for the preparation of assessments of the state of Earth's climate system. The construction of the ocean thermal analyses used in this work was supported by grants from the NOAA Climate and Global Change program. Preparation of the integrated ocean databases used in this work was supported by the NOAA, NOAA/NASA, and NOAA/DOE Climate and Global Change programs and by the NOAA Environmental Services Data and Information Management program. J.I.A. is a University Corporation for Atmospheric Research Project Scientist at NODC/NOAA.

11 December 2000; accepted 2 March 2001

Detection of Anthropogenic Climate Change in the World's Oceans

Tim P. Barnett,* David W. Pierce, Reiner Schnur

Large-scale increases in the heat content of the world's oceans have been observed to occur over the last 45 years. The horizontal and temporal character of these changes has been closely replicated by the state-of-the-art Parallel Climate Model (PCM) forced by observed and estimated anthropogenic gases. Application of optimal detection methodology shows that the model-produced signals are indistinguishable from the observations at the 0.05 confidence level. Further, the chances of either the anthropogenic or observed signals being produced by the PCM as a result of natural, internal forcing alone are less than 5%. This suggests that the observed ocean heat-content changes are consistent with those expected from anthropogenic forcing, which broadens the basis for claims that an anthropogenic signal has been detected in the global climate system. Additionally, the requirement that modeled ocean heat uptakes match observations puts a strong, new constraint on anthropogenically forced climate models. It is unknown if the current generation of climate models, other than the PCM, meet this constraint.

Almost all rigorous studies attempting to find the impact of anthropogenic forcing in today's climate system have used air-temperature observations as the data set of choice for the detection study (*1*). These studies most often use near-surface air temperature [e.g., (*2–6*)]. Changes in sea ice (*7*) and the vertical temperature structure of the atmosphere obtained from radiosonde data (*8–11*) have also been investigated for evidence of an anthropogenic signal.

Climate models predict that there will be substantial anthropogenic changes in variables only weakly related to near-surface air temperature. For example, model-predicted signals have been detected in the magnitude of the annual cycle and wintertime diurnal temperature ranges (*12*), but there are few such studies at present. It seems imperative that statements about the detection and attribution of model-predicted anthropogenic climate change, such as made in the most recent Intergovernmental Panel on Climate Change (IPCC) Assessment (*13*), be placed on a stronger foundation by quantitatively identifying such signals in other elements of the climate system.

A major component of the global climate system is the oceans; covering roughly 72% of the planet's surface, they have the thermal inertia and heat capacity to help maintain and ameliorate climate variability. Although the surface temperature of the oceans has been used in detection and attribution studies, apparently no attempt has been made to use changes in temperature at depth. A recent observational study (*14*) has shown that the heat content of the upper ocean has been increasing over the last 45 years in all the world's oceans, although the warming rate varies considerably among different ocean basins. We show in this

Climate Research Division, Scripps Institution of Oceanography, University of California, San Diego, La Jolla, CA 92093, USA.

*To whom correspondence should be addressed. E-mail: tbarnett@ucsd.edu

study that at least one global climate model, forced by a combination of observed and estimated anthropogenic gases, has reproduced the observed changes in ocean heat content with surprising accuracy.

The decadal changes over the last 45 years in the heat content of the upper 3000 m of the water column estimated from observations are shown in Fig. 1 (*14*). Only the very low frequency component of the signal is of interest here, so we chose to work relative to this depth and use decadal averages to filter out noise associated with eddies and interannual or decadal natural variability. A similar set of heat-content changes, relative to a 300-year control run climate, was computed from five different realizations of the Parallel Climate Model (PCM) forced by observed and estimated concentrations of greenhouse gases and the direct effect of sulfate aerosols on the atmosphere (*15*). This state-of-the-art global climate model, which uses no flux-correction scheme, is a cooperative effort between a number of universities and government laboratories in the United States (*16*). A brief summary of the model components, forcing scenarios, and current results are given in (*17–19*), while a more detailed description can be found at www.cgd.ucar.edu/pcm.

Figure 1 shows an unexpectedly close correspondence between the observed heat-content change and the average of the same quantity from the five model realizations. These results were obtained by subsampling the model data at the same locations and times where observations existed (*20*). When the scatter between the multiple model runs is included (shaded regions on Fig. 1), it becomes apparent that there is little or no significant difference between model and observations, even though the heat-content changes vary among ocean basins. The main exception occurs in the 1970s, when the observations show a decadal anomaly that the model runs do not reproduce. We speculate that the anomaly is associated with the apparent regime-like shift in the North Pacific Oscillation and other regional climate modes that occurred at that time (*21–24*). It is not possible, given the manner in which it was forced, that the model could have captured this specific decadal signal. However, the model does produce, in both its anthropogenically forced runs and control run, decadal fluctuations that have the same magnitude and time scale as those associated with the observed anomaly of the 1970s. In any event, the anomaly does not alter the close correspondence between model and observations.

In summary, the PCM, forced by anthropogenic constituents, produced changes in heat content in each of the major oceans over the last 45 years that are highly similar to those observed.

The vertical development of the oceanic warming signal in the PCM for the world's oceans is shown in Fig. 2. Here we show the time evolution, from the start of the integrations (1870) through the year 2000, for the average of the five-member ensemble. The scatter among the five realizations allowed us to estimate a standard deviation that was used to filter the results so that temperature anomalies exceeding a 90% confidence limit are indicated by the gray shaded areas.

The nature of the warming in the various oceans is markedly different. The Atlantic, particularly the South Atlantic, shows strong vertical convection taking the signal to depth

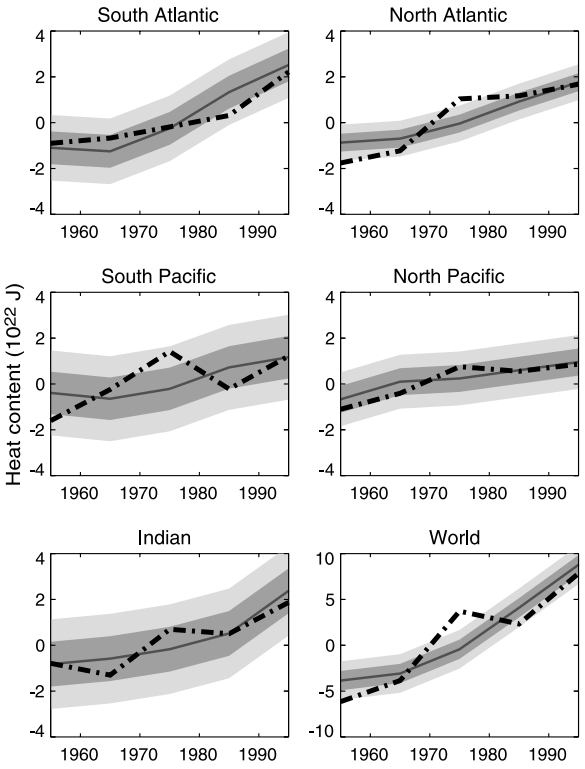

Fig. 1. Decadal values of anomalous heat content (10^{22} J) in various ocean basins. The heavy dashed line is from observations (*14*), and the solid line is the average from five realizations of the PCM (*16–19*) forced by observed and estimated anthropogenic forcing. Both curves show significant warming in all basins since the 1950s. The shaded bands denote one (heavy shading) and two (light shading) standard deviations about the model mean signal estimated from the standard deviation in the scatter of the five-member ensemble. The heat content is computed over the upper 3000 m of the water column. The space/time sampling was identical for both model and observations. Basin averages for the northern oceans are defined between 60°N and the equator. The southern ocean averages are between the equator and 77°S.

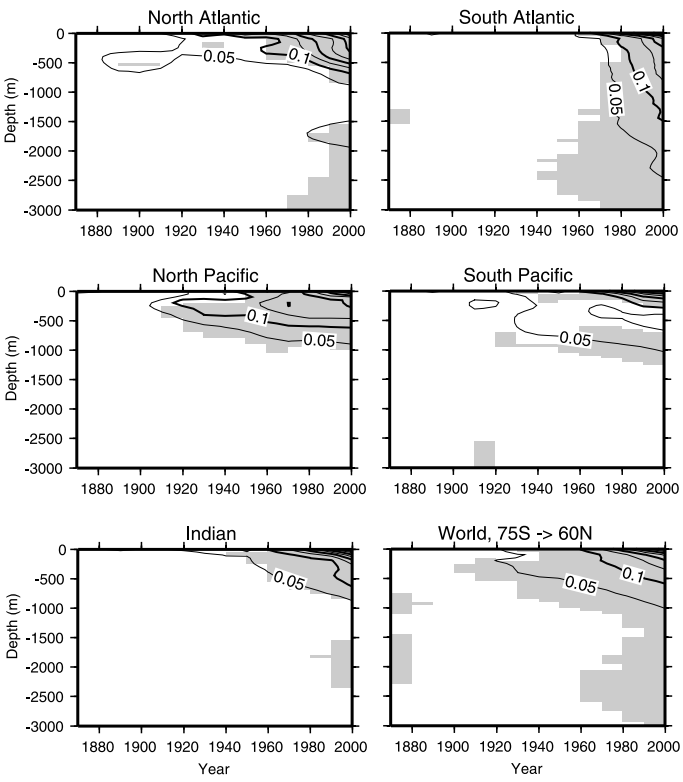

Fig. 2. Decadal temperature anomalies (°C) in various ocean basins since 1870 from the PCM. Gray-shaded regions indicate signals statistically distinguishable from zero. The timing of the warming, as well as its vertical structure, varies substantially among the basins. The deep changes in the "World" oceans are seen to be derived solely from changes in the Atlantic. The contour interval is 0.05°C.

quite rapidly. The South Atlantic regional average includes portions of the model's deep-water formation region in the Weddell Sea, so the rapid penetration to depth is expected. The signal is larger in the North Atlantic, but does not appear to penetrate as rapidly, possibly because the regional averaging area in that ocean is large relative to the space scales of deep vertical mixing. In the other oceans, the signal is more consistent with what one would expect from a purely diffusive process. It is important to note that there is little deep water formed in the South Pacific regional average, which otherwise would be expected to resemble the South Atlantic regional average. At any rate, it is apparent that the signal in the deep ocean labeled "world" oceans comes from the Atlantic in the model simulations.

The temporal evolution of the model's vertical temperature structure is compared with observations in Fig. 3, for the North Pacific and North Atlantic Oceans. These are oceans where the data density is highest. In this case, we have concentrated on temperature changes in the upper 2000 m to emphasize the region of maximal signal strength and applied the model-derived significance factors used in Fig. 2 to filter noise from the data.

In the North Atlantic, the observations show a near-surface warming since about 1980, whereas the model begins warming at about 1950. This result may be partially due to the presence of a single, noisy observation set compared with the smoother, ensemble average. However, the penetration of warming with time and depth is otherwise similar between the model and observations. The more-or-less diffusive penetration in the North Pacific is captured in the model, although the very near-surface structure is again somewhat different. These discrepancies in near-surface behavior may be due to the large interannual and decadal variability that the model, running with no real-world input, cannot be expected to capture (unless it were to be forced by the observed fluxes of heat, momentum, and moisture). The model also contains no natural external forcings such as solar or volcanic mechanisms (*25*). The key point is that the substantial differences in the way the observed warming has penetrated to depth in the two oceans is reasonably well captured by the PCM, albeit with the caveats noted above.

We examined whether the model-produced changes in ocean heat content are different from those expected by chance, e.g., different from those expected in a long control run of the PCM. This indicates whether a significant climate change has been observed in the forced model runs. We further examined whether the model-produced changes are statistically consistent with the observations. The first question addresses the detection of climate change, whereas the second examines whether anthropogenic forcing could be responsible for the observed changes.

The detection and attribution method that we use here is termed "optimal detection" and is well documented (*3*, *26–28*). The basic idea is to compute the space/time pattern of change predicted by the model—the anthropogenic fingerprint—and its strength. Normalization of the data before estimating these signals by the natural variability or noise, determined from one of two PCM control runs (300 years long), is necessary for "optimal" detection (*29*, *30*). The space/time distribution of the observations are projected onto this "fingerprint," and the observed pattern strength estimated. We then used the second PCM control run (270 years long) to estimate the level of expected natural variability under conditions where no anthropogenic forcing exists. This latter information allows us to estimate a confidence level on the observations and thus make significance statements about difference between the observed signal strength and the model-predicted signal strength (*31*)

The analysis showed that a single space/time pattern or fingerprint captured the model's anthropogenic signal well enough that both the optimal and nonoptimal detection analyses gave basically the same result. From here on, we use a nonoptimal analysis so that both control runs can be used to estimate levels of natural variability. The signal strength of this pattern from each of the five realizations and their mean value are shown in Fig. 4. Also shown is the signal strength for the observations projected onto the model fingerprint. The projection of the control run data onto this fingerprint allows a noise estimate for computing significance. These latter values were expressed as 95% confidence intervals and centered on the mean model value to facilitate discussion (stippled region).

The confidence limits do not include the origin (the "no signal" or no climate change

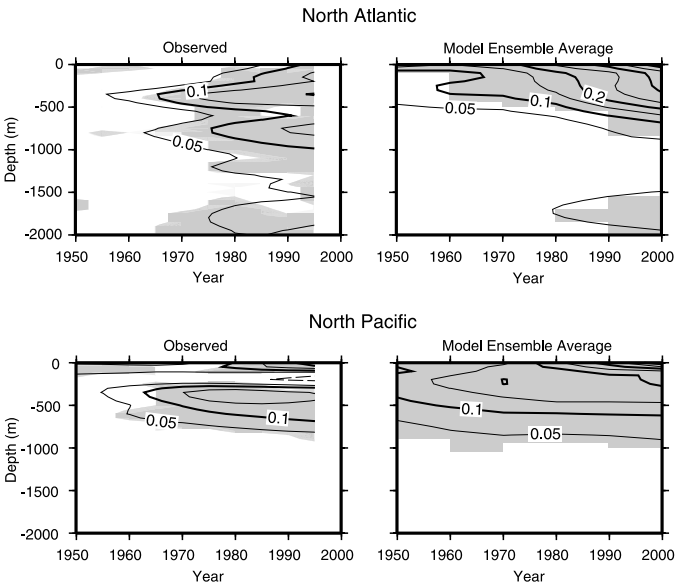

Fig. 3. Modeled and observed temporal and vertical changes in the temperature in the upper 2000 m of the data-rich North Pacific and North Atlantic Oceans. Near the surface, where interannual and decadal changes and external forcings strongly affect the thermal structure, any agreement is largely due to chance. Gray-shaded regions denote areas where changes are statistically different from zero. The model broadly reproduces the main features of the vertical structure and its temporal evolution over the last 40 years. The contour interval is 0.05°C.

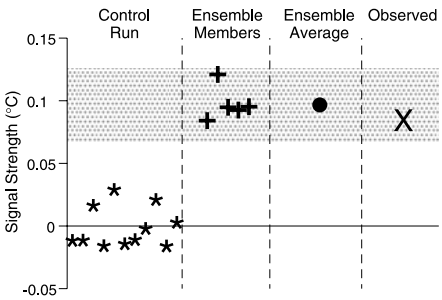

Fig. 4. Detection and attribution diagram. The strength of the anthropogenic pattern of model-predicted changes in depth-averaged ocean temperatures (°C) is shown for each of the five realizations (+) and their ensemble average (●). Also shown is the strength of the model-predicted signal in the observations (X). The lightly stippled region corresponds to the 95% confidence region, centered on the ensemble average, associated with natural variability as estimated from the PCM control runs [see (*31*)]. The individual signal-strength estimates for independent 45-year chunks of the control run are indicated (★). All forced runs, their mean, and the observations fall within the 95% confidence region and so are indistinguishable from each other, i.e., the model-produced signal and the observations are "consistent" with each other. The uncertainty region does not include the origin, so that natural variability, as estimated by the model, cannot explain the signal in the observations. The results are for the nonoptimal detection method, but do not differ appreciably from that for the full optimal approach.

case), and so the mean of the anthropogenic runs is highly significant and detection of a climate change signal in the model has occurred, i.e., the mean is not expected to occur by chance in the control run. Further, the differences between the various model runs and the observed state all fall within the confidence limits, so that we cannot distinguish between any of the five realizations or the observations. They are all identical from a statistical point of view. Hence, we say that the observations are consistent with the anthropogenically forced model results. This suggests, with confidence exceeding 95%, that one may accept anthropogenic forcing as one possible explanation for the observed changes in heat content of the global oceans. There may be other possible explanations that were not included in the model simulations—hence the word "consistent" used above.

The work reported here yields strong results, but some caveats are necessary. The observational data are sparse in the southern oceans before the 1980s, which should be kept in mind when comparing the observations with the model and when using model and observed data from these regions in a detection methodology. However, our subsampling method of using model data only where comparable observations occurred should largely overcome this problem for detection purposes. Finally, the estimates of natural variability used in the detection work were derived from simulations—not observations, which do not exist in sufficient quantity for this purpose.

A very low frequency variability, perhaps drift, can be seen in the model control run that varied in magnitude and sign from ocean to ocean. The time scale of this variability was on the order of hundreds of years, much longer than the 45-year time slices used in this study. Sensitivity studies suggest that it has not affected our analysis. We suggest that the control run be extended to an order of 1000 years in future studies, as has been done by other centers, to better evaluate natural variability in the model and the role of ultralow-frequency change. In addition, the forced runs we used for detection did not include indirect sulfate, ozone, so-called black aerosols, and other anthropogenic factors, nor did they include external forcing due to solar variability and volcanic activity [e.g., (*25*)]. Most of the excluded factors introduce a cooling that might negate the fact that the model is a little too warm.

The detection and attribution study used regional and vertical averages. A more complete analysis should consider the full three-dimensional structure of the signal and noise fields. Such an analysis is currently in progress, although we do not expect it to change the major conclusions presented here. Further confirmation of our results comes from a similar analysis of anthropogenically forced runs at the Max Planck Institute in Hamburg, Germany (*32*).

Perhaps the most important aspect of this work is that it establishes a strong constraint on the performance and veracity of anthropogenically forced climate models. For example, a climate model that reproduces the observed change in global air temperature over the last 50 years, but fails to quantitatively reproduce the observed changed in ocean heat content, cannot be correct. The PCM has a relatively low sensitivity (less anthropogenic impact on climate) and captures both the ocean- and air-temperature changes. It seems likely that models with higher sensitivity, those predicting the most drastic anthropogenic climate changes in the future, may have difficulty satisfying the ocean constraint. To our knowledge, the PCM is the only model currently able to do this and still accurately reflect the changes in surface air temperature over the last 50 years. Future studies should take into account the ocean constraint when deciding which future climate summaries are most reliable.

References and Notes

1. For examples of previous detection studies, see J. F. B. Mitchell, D. J. Karoly, in *IPCC WGI Third Assessment Report*, J. T. Houghton *et al.*, Eds. (Cambridge Univ. Press, Cambridge, 2001), chap. 12.
2. G. C. Hegerl *et al.*, *J. Clim.* **9**, 2281 (1996).
3. G. C. Hegerl *et al. Clim. Dyn.* **13**, 613 (1997).
4. G. C. Hegerl *et al.*, *Clim. Dyn*. **16**, 737 (2000).
5. T. P. Barnett *et al.*, *Bull. Am. Meteorol. Soc*. **80**, 2631 (1999).
6. S. F. B. Tett *et al.*, *J. Geophys. Res*., in preparation.
7. K. Y. Vinnikov *et al.*, *Science* **286**, 1934 (1999).
8. S. F. B. Tett, J. F. B. Mitchell, D. E. Parker, M. R. Allen, *Science* **274**, 170 (1996).
9. D. E. Parker, M. R. Allen, *Science* **274**, 170 (1996).
10. B. D. Santer *et al.*, *Nature* **384**, 524 (1996).
11. B. D. Santer *et al*., *Nature* **382**, 39 (1996).
12. R. Schnur, *Rep. No. 314* (Max-Planck-Institut für Meteorologie, Hamburg, Germany, 2000).
13. *IPCC WGI Third Assessment Report*, J. T. Houghton *et al.*, Eds. (Cambridge Univ. Press, Cambridge, 2001).
14. S. Levitus, J. I. Antonov, T. P. Boyer, C. Stephens, *Science* **287**, 222 (2000).
15. The five anthropogenic runs were started from different points in the control run separated by 10 years. The forcing was prescribed according to observed and projected estimates of the concentration of greenhouse gases and the direct effect of sulfate aerosols. See (*17*) for details of these runs and their forcing. Each run lasted from 1870 to 2000. We subtracted from each run the corresponding 130-year section of the control run. This effectively created anomalies and removed ultralow-frequency variability and/or consistent model drift from the subsequent analysis.
16. W. M. Washington *et al.*, *Clim. Dyn*. **16**, 755 (2000).
17. A. Dai, T. M. L. Wigley, B. A. Boville, J. T. Kiehl, L. E. Buja, *J. Clim.* **14**, 485 (2001).
18. A. Dai *et. al*., *Bull. Am. Meteorol. Soc.*, in preparation.
19. The atmospheric component of the PCM is the CCM3 atmospheric general circulation model (AGCM) developed at the National Center for Atmospheric Research (NCAR) and is used at T42 resolution (about 280 km by 280 km grid). The CCM3 includes a land surface model that accounts for soil moisture, vegetation types, and so forth. The University of Texas (Austin) parallel river transport model is a new component of the PCM and is designed to match the resolution of the atmospheric model. The ocean component of PCM is the Parallel Ocean Program (POP) model developed jointly by Los Alamos National Laboratory, Naval Postgraduate School (NPS), and NCAR. This model has unusually high spatial resolution for an anthropogenic scenario integration, with grid spacing of about 0.67° latitude/longitude except near the equator, where the grid interval is 0.5°. The final major model component of PCM is a sea-ice model developed by Y. Zhang at NPS, which has a 27-km resolution and uses an elastic-viscous-plastic formulation. The sea-ice formulation treatment is especially important for reproducing a realistic feedback mechanism between sea-ice processes and climate-change forcings. The model uses no flux corrections. Full references and further details of the model can be found at www.cgd.ucar.edu/pcm.
20. The model and Levitus (*14*) data set were interpolated onto a common grid. Each model grid point was sampled only if there was a nonzero value in the Levitus grid point fields (the "gp" set), indicating the influence of an observation; other locations were set to climatology. Thus, the observed and model-predicted heat-content changes were computed in exactly the same manner. Full sampling of the model grid indicated little change in the results, especially after 1970. In the northern oceans, there was no change due to the heavier sampling in those oceans. Indeed, the "gp" coverage after 1956 to a depth of 3000 m is typically 80 to 90% by volume in all basins, with the exception of the South Pacific, where it varies between 60 and 80% for the period 1975 to 1990, before returning to above 90%. The role of ocean eddies in this data set is one of uncorrelated, quasi-random noise. The spatiotemporal smoothing used in this study effectively eliminates eddy contamination.
21. E. L. Venrick, J. A. McGowan, D. R. Cayan, T. L. Hayward, *Science* **238**, 70 (1987).
22. M. Latif, T. Barnett, *Science* **266**, 634 (1994).
23. D. W. Pierce, T. P. Barnett, M. Latif, *J. Clim.* **13**, 1173 (2000).
24. J. Mantua *et al.*, *Bull. Am. Meteorol. Soc.* **78**, 1069 (1997).
25. P. A. Stott *et al.*, *Science* **290**, 2133 (2000).
26. G. C. Hegerl *et al.*, *J. Clim.* **9**, 2281 (1996).
27. S. F. B. Tett, P. A. Stott, M. R. Allen, M. J. Ingram, J. F. B. Mitchell, *Nature* **399**, 569 (1999).
28. M. R. Allen, S. F. B. Tett, *Clim. Dyn*. **15**, 419 (1999).
29. K. Hasselmann, *J. Clim.* **6**, 1957 (1993).
30. The noise was estimated from the control-run heat-content values after removing a quadratic fit to the 300 years of record for each basin. The changes in heat content on time scales of 50 years were not affected by removal of this ultralow-frequency variability. The detection analyses described in (*31*) were done with and without this filtering. In the case of no filtering, i.e., the low-frequency signal left in the data, the distribution of heat-change estimates was strongly biased negatively, i.e., toward ocean cooling. This analysis made the detection significance statements unrealistically strong in our view. Analysis with the low frequency removed resulted in detection statements that, although still strong, we believe are much more conservative than those made with the low-frequency changes left in the data. We also removed a simple trend fit, instead of the quadratic, and found that the results were not affected.
31. The detection data consisted of five decadal values of anomalous heat content for each of six ocean basins. These data were concatenated for each of the five realizations, giving a total of five series each 30 ($=5 \times 6$) terms in length. These series include the space and time variations of the heat content for each realization as in (*28*). The data were both (i) weighted by the appropriate noise estimate derived from the control run for an optimal detection and (ii) left unweighted. The covariance of either of these data were computed by using true ensemble-averaging techniques. The leading empirical orthogonal function (EOF) of these covariance matrices accounted for 87% of the data set variance and is referred to in the text as the anthropogenic "signal." The second and higher EOFs in either case were statistically degenerate and not considered further. The associated principal components give the strength of the model's anthropogenic signal. The dot product of the observations, weighted (or unweighted) as noted above, and the signal gave the "observed" strength of

the signal. The significance of these estimates was tested against nonoverlapping 45-year-long slices of data derived from the control run, i.e., against the hypothesis that the heat-content changes in the anthropogenic runs could have occurred as a result of natural, internal variability in the absence of any anthropogenic forcing. Forty-five-year chunks of the control run data were processed just as the observations and five anthropogenic realizations were processed, and then projected onto the signal. The results show that the signal strengths of the five realizations and observations are quantitatively similar and nonzero relative to the uncertainty of the natural variability of the model, i.e., the model and observed projections are statistically consistent and not expected to occur as a result of internal model variability. The confidence associated with this statement exceeds 95%. With no variance weighting, i.e., nonoptimal detection, the results were essentially identical, if not a little stronger than in the optimal case.

32. B. Reichert, L. Bengtsson, R. Schnur, in preparation.
33. Supported by the National Oceanographic and Atmospheric Association Climate Change Data and Detection program and the U.S. Department of Energy, Office of Energy Research, as part of the International ad hoc Detection Group effort. Additional support from the U.S. Department of Energy (grant DE-FG03-98ER62505), the National Science Foundation (grant ATM-9901110), and the Scripps Institution is gratefully acknowledged. R.S. was partially supported by the European Commission under contract ENV4-CT97-0501. We are particularly indebted to the PCM group, headed by W. Washington, for their assistance and generosity with their model data and to S. Levitus and coauthors, whose earlier work gave rise to this study. Technical discussions with M. Allen, T. Delworth, and anonymous reviewers greatly improved the manuscript.

14 December 2000; accepted 7 March 2001

Climate Response to Orbital Forcing Across the Oligocene-Miocene Boundary

James C. Zachos,[1]* Nicholas J. Shackleton,[2] Justin S. Revenaugh,[1] Heiko Pälike,[2] Benjamin P. Flower[3]

Spectral analyses of an uninterrupted 5.5-million-year (My)–long chronology of late Oligocene–early Miocene climate and ocean carbon chemistry from two deep-sea cores recovered in the western equatorial Atlantic reveal variance concentrated at all Milankovitch frequencies. Exceptional spectral power in climate is recorded at the 406-thousand-year (ky) period eccentricity band over a 3.4-million-year period [20 to 23.4 My ago (Ma)] as well as in the 125- and 95-ky bands over a 1.3-million-year period (21.7 to 23.0 Ma) of suspected low greenhouse gas levels. Moreover, a major transient glaciation at the epoch boundary (~23 Ma), Mi-1, corresponds with a rare orbital congruence involving obliquity and eccentricity. The anomaly, which consists of low-amplitude variance in obliquity (a node) and a minimum in eccentricity, results in an extended period (~200 ky) of low seasonality orbits favorable to ice-sheet expansion on Antarctica.

Orbital dynamics are thought to have driven Quaternary climate change, but their effects in earlier times when climate boundary conditions differed have been difficult to resolve. Here, we examine the late Oligocene and early Miocene (~20.0 to 25.5 Ma), a time when Antarctica was either ice-free or only partially glaciated, using a 5.5-My-long high-fidelity benthic foraminiferal stable isotope record. This record is a composite constructed largely with newly collected data from Ocean Drilling Program (ODP) Site 926, Ceara Rise (3°43′N, 42°54′W), as well as data from Site 929. Sedimentation rates at Site 926, which is located at a depth of 3598 m where carbonate dissolution is reduced, are as much as 50% higher than at Site 929 and other deeper sites (*1*).

We use the age model of Shackleton and colleagues (*2*) for our isotope records. They calibrated proxy records of Oligocene and Miocene lithologic cycles, including magnetic susceptibility (MS), in the Leg 154 cores (*3*) to an orbital curve (*4*) using modern values for tidal dissipation and dynamical ellipticity (*5*). They achieved an absolute calibration by pattern matching the 400-ky cycles of eccentricity-modulated precession in MS with similar cycles in the target curve. They then used individual obliquity maxima to establish the fine-scale tuning and verified this by comparing the 1.2-My amplitude modulation of obliquity in the data. The astronomical age derived for the Oligocene-Miocene (O/M) boundary, as recognized by the presence of *Sphenolithus delphix* and a positive carbon isotope anomaly of 0.65‰, is roughly 700 ky younger than that established in the radiometric calibrated time scale (*6*).

We developed high-resolution (~3.7 ky) carbon and oxygen isotope records for benthic foraminifera specimens collected from Hole 926B (*7*). Our records match those for Hole 929A (*8*) for each cycle down to the obliquity level over the interval of overlap (926B, 20.0 to 25.2 Ma; 929, 20.5 to 25.4 Ma) (Fig. 1A). The only noticeable differences are the higher frequency oscillations present in the 926 record (e.g., precession) that are not resolved at Site 929 because of lower sedimentation rates (26 m/My for Hole 926B versus 19 m/My for Hole 929A across the O/M boundary). The ranges of isotope values are similar despite the nearly 1 km difference in water depth between sites. This similarity implies that the deep water in this part of the Atlantic was chemically homogeneous over much of this period and that a large portion of the variance in the isotopic record is signal.

The most prominent feature of the records is a positive excursion in $\delta^{18}O$ coupled with a positive shift in $\delta^{13}C$ values at 23.0 Ma, the Mi-1 excursion. This event, which can be distinguished in other deep-sea $\delta^{18}O$ records (*9*), is characterized by a series of obliquity period cycles beginning at 23.3 Ma over which $\delta^{18}O$ increase, to a peak at ~23.0 Ma. This peak is followed by a series of three declining cycles (deglaciations) over the next ~150,000 years. Thereafter, the cycles appear to be predominantly 100 ky. A second, but weaker, positive $\delta^{18}O$ excursion occurs at 21 Ma. The $\delta^{13}C$ values show low-frequency cycles that increase in amplitude and value, eventually peaking from 23.0 to 21.6 Ma, after which they decline.

To ascertain the nature of the high-frequency signals in the isotope records, we first built composite $\delta^{18}O$ and $\delta^{13}C$ time series by splicing gaps in the Hole 926B records with grafts from the Hole 929A records [Web table 1 (*10*)]. We then applied band-pass gaussian filters to each isotope record as well as the orbital calculations and MS to extract oscillations associated with 400-, 100-, and 41-ky cycles [AnalySeries (*11*)] (Fig. 1B). In the 400-ky band, both the $\delta^{13}C$ and $\delta^{18}O$ filters co-vary with the 400-ky filter of eccentricity, in that they appear phase-locked between 20 to 24 Ma. Also, the 400-ky eccentricity-related amplitude modulation of $\delta^{13}C$, and to a lesser extent $\delta^{18}O$, exhibits a pattern similar to that of the orbital modulation, including subtle peaks near ~21.4 and 23.0 Ma (Fig. 1B). The amplitude of the 400-ky filter of $\delta^{18}O$ increases only after 23.4 Ma, just below the O/M boundary. This is the

[1]Earth Sciences Department, Center for Dynamics and Evolution of the Land-Sea Interface, University of California, Santa Cruz, CA 95064, USA. [2]Godwin Laboratory for Quaternary Studies, Cambridge University, Cambridge CB2 3SA, UK. [3]College of Marine Science, University of South Florida, St. Petersburg, FL 33701, USA.

*To whom correspondence should be addressed. E-mail: jzachos@es.ucsc.edu